THE JOURNAL OF PHYSICAL CHEMISTRY C
A JOURNAL OF THE AMERICAN CHEMICAL SOCIETY

pubs.acs.org/JPCC

Article

Nanoimaging of Water Bending and Carboxylate Stretching Modes in Colloidal Nanocrystal Films

Wassie M. Takele and Terefe G. Habteyes*

Cite This: J. Phys. Chem. C 2024, 128, 2052−2061

Read Online

ACCESS | Metrics & More | Article Recommendations | Supporting Information

ABSTRACT: In this study, we utilize scattering-type scanning near-field optical microscopy combined with a tunable infrared quantum cascade laser to achieve nanoscale imaging of vibrational modes within colloidal nanocrystal films under ambient conditions. We focus on the characterization of the bending mode of water and the stretching modes of carboxylates in films composed of gold nanocrystals (AuNCs) coated with trisodium citrate (Na_3Cit) ligands. Our approach enables the spatial resolution of vibrational spectra, revealing a line width for the water bending mode of less than 3 cm^{-1}, a value notably consistent with that found in gas-phase spectra. Intriguingly, our detailed analysis of the near-field spectra discriminates among three overlapping domains: the film−air interface, the internal layers of the film, and the film−substrate boundary. Further investigation into the citrate stretching modes elucidates three structural domains differentiated by their spatial relation to the AuNCs and the film's thickness. Our results challenge previous understandings by demonstrating that a particular vibrational band, formerly attributed to surface-bound carboxylates, is in fact a signature of higher-order structures in dense Na_3Cit aggregates. Complementary surface-enhanced Raman spectroscopy measurements indicate that citrate's interaction with the nanocrystal surface is intricately modulated by sodium ions and water molecules. These experimental observations are further supported and explained by theoretical insights from density functional theory calculations. Collectively, our findings not only present a more nuanced view of the interactions within these complex nanoscale systems but also pave the way for a deeper understanding of surface chemistry and interfacial phenomena at the molecular level.

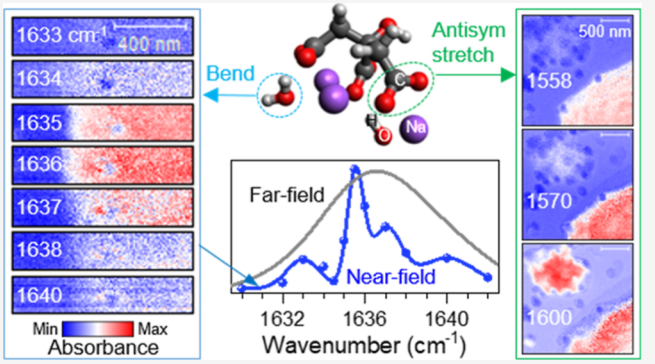

1. INTRODUCTION

As the most important solvent and medium in both chemistry and biology, water has long been the subject of vibrational spectroscopic analysis aimed at understanding its intermolecular interactions.[1−6] A water molecule exhibits three vibrational modes—symmetric stretch, antisymmetric stretch, and bend—whose peak frequencies and spectral line widths are sensitive to the extent of these interactions and environments.[7−9] For the most extensively studied stretching mode, the peak frequency decreases due to hydrogen bonding, and the line width of the vibrational band narrows from about 80 cm^{-1} in bulk water[7] to approximately 10 cm^{-1} at the water surface[2] and gas phase cluster[6] and further to 3 cm^{-1} in rotationally resolved gas-phase spectra.[10] For the bending mode, the frequency appearing at 1595 cm^{-1} in the gas phase shifts upward in bulk water, indicating an effect of hydrogen bonding opposite to that observed for the stretching mode frequency.[11] While existing studies provide a foundational understanding of hydrogen bonding, the systematic exploration of water molecules' vibrational behaviors in thin films remains incomplete. Water molecules are believed to be omnipresent on surfaces and within solid films derived from the solvent evaporation of aqueous solutions. Notably, water serves as the predominant solvent in the colloidal synthesis of metal nanocrystals (NCs). Its presence and behavior in solid films carry significant implications for various applications, including heterogeneous catalysis and surface-enhanced spectroscopy. This study focuses on the real-space mapping of vibrational modes of water molecules and surface ligands within a solid film of colloidal gold nanocrystals (AuNCs).

Surface ligands play an indispensable role in the formation and stabilization of colloidal inorganic NCs.[12,13] They are essential during crystal growth in solution and are necessary for maintaining post-synthetic NC stability. Beyond these foundational roles, surface ligands also serve as active modulators of NCs' physicochemical properties,[14−23] thereby expanding their applicability across diverse fields such as heterogeneous catalysis,[24] biomedical imaging,[25] and surface-enhanced spec-

Received: November 22, 2023
Revised: January 9, 2024
Accepted: January 15, 2024
Published: January 29, 2024

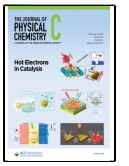

https://doi.org/10.1021/acs.jpcc.3c07693
J. Phys. Chem. C 2024, 128, 2052−2061

troscopy.[26] While it has long been believed that surface ligands might impede catalytic activities, recent studies have upended this view by showing that these ligands can actually boost catalytic efficiencies and enhance product selectivity,[15,16] particularly in plasmon-enhanced photocatalysis.[27−30]

In various applications, such as surface-enhanced Raman scattering (SERS) spectroscopy and heterogeneous catalysis, NCs are commonly assembled onto solid surfaces. It is often assumed that excess surface ligands must be removed for optimal performance. However, entirely removing these ligands is impractical; doing so compromises the stability of the NCs beyond a certain concentration threshold. Consequently, the resulting solid films typically comprise not just the NCs but also the aggregates of excess surface ligands and trapped solvent molecules, such as water. To investigate the role and properties of surface ligands, multiple analytical techniques have been utilized, including attenuated total reflectance infrared (ATR-IR) spectroscopy,[31] sum-frequency generation,[32−35] X-ray photoelectron spectroscopy,[31,36] and solid-state nuclear magnetic resonance.[37,38] These methods, however, are limited in their spatial resolution, which hampers our ability to distinguish whether the observed signals emanate from molecules directly adsorbed onto the NC surface or from distant aggregates. While SERS shows promise in detecting molecules in close proximity to the NC surface,[39,40] it cannot offer a complete characterization of heterogeneous films that might contain both NC aggregates and excess ligands. As a result, real-space mapping of surface ligands and water molecules trapped in a heterogeneous film of colloidal NCs has not been reported.

In this work, we employ scattering-type scanning near-field optical microscopy (s-SNOM) coupled with a tunable IR quantum cascade laser (QCL) to image both the water bending and carboxylate stretching modes in real space. In previous research, s-SNOM has been employed to map a range of excitations including plasmons,[41−47] polaritons,[48−51] vibrational modes,[52−57] and aging effects.[58] Recently, vibrational imaging utilizing s-SNOM has been applied for visualizing the growth of water films from water vapor on hydrophilic mineral nanoparticles[59] as well as probing the bending mode of water in the solution phase through the SiN membrane.[60] The findings presented here demonstrate the applicability of the s-SNOM vibrational imaging of water molecules and surface ligands in solid thin films. These observations are made within thin films composed of colloidal AuNCs coated with trisodium citrate (Na_3Cit) surface ligands. Our spatiospectral imaging reveals that the line width of the water bending mode is less than 3 cm^{-1}, surprisingly in agreement with the values seen in rotationally resolved gas-phase vibrational spectra.[10] Close observation of the near-field spectra for the bending mode also identifies three partially resolved domains, which can be attributed to the film−air interface, the inner layer, and the film−substrate interface. While probing the citrate stretching mode, we discovered three distinct structural domains that vary based on their proximity to the AuNCs and the thickness of the Na_3Cit film. Contrary to previous assignments, we find that a vibrational band, initially thought to be related to surface-bound carboxylates, actually originates from higher-order structures in relatively thick Na_3Cit aggregates. Vibrational resonances due to surface and subsurface structures are identified. Utilizing SERS, we ascertain that the interaction of citrate with the nanocrystal surface is mediated by sodium cations and water molecules. These spectral assignments are corroborated by density functional theory (DFT) calculations.

2. EXPERIMENTAL METHODS

2.1. Preparation of Thin Films of Trisodium Citrate-Capped AuNCs. A 500 μL aliquot of an aqueous solution of trisodium citrate-capped gold nanocrystals (AuNCs/Na_3Cit, ∼40 nm diameter, Nanopartz, Inc.) was diluted to 2 mL in deionized water and centrifuged at 7000 rpm for 5 min. The supernatant solution was carefully removed using a pipet, leaving the AuNCs/Na_3Cit precipitate, which was then diluted to 200 μL in deionized water. Twenty μL of this solution was drop-cast on a silicon substrate that had been cleaned by consecutive sonication for 5 min each in acetone, 2-propanol, and deionized water.

2.2. Far-Field Spectroscopy Measurments. ATR-IR spectra of the solid AuNCs/Na_3Cit film were recorded using a Bruker Alpha-P total-reflectance IR (diamond ATR) spectrometer. The spectra were collected in the 4000−500 cm^{-1} window with a resolution of 4 cm^{-1}. SERS spectroscopy was carried out at 633 nm excitation using a modified Olympus inverted microscope with a dark-field objective of 0.9 NA and 100× magnification. The spectra were obtained by directing the signal to the IsoPlane Spectrograph of Princeton Instruments, equipped with a thermoelectrically cooled (−75 °C) charge-coupled device camera. About 90% of the light collected from the sample by the objective was sent to the spectrometer, while the remaining signal was directed to an Olympus UC30 camera attached to the microscope.

2.3. Vibrational Imaging Using s-SNOM. s-SNOM vibrational imaging is carried out utilizing an atomic force microscope (AFM)/near-field platform (Neaspec, part of attocube systems) with broadly tunable IR as excitation source, as described in earlier publications[43,55] (see schematics of the setup in Figure S1). A QCL (MIRcat-QT-Z-2400 of Daylight Solutions) is used to generate linearly polarized IR radiation with a tunable frequency and about ∼0.1 cm^{-1} resolution. The AFM operates in noncontact tapping mode, employing a metal-coated probe (Arrow NCPt) with a resonance frequency $\Omega \approx 270$ kHz. The vertically polarized output of the QCL is focused at the tip−sample junction using a parabolic mirror (NA ∼ 0.46) at a 30° angle of incidence with respect to the sample plane. Laser power is maintained at 3 mW across all QCL frequencies through the use of dual polarizers. Photons scattered from the nanoscale region of tip−sample near-field interaction are detected using HgCdTe photodiodes cooled with liquid nitrogen. The far-field background signal is removed using pseudoheterodyne interferometric detection[61] and signal demodulation at a frequency of 4 Ω. This detection scheme simultaneously captures both the scattering amplitude and the phase, which are related to the real and imaginary parts of the dielectric function of materials. It is important to note that for any solid and liquid, the real and imaginary parts of the dielectric function are related through the Kramers−Kronig relations at all frequencies.[62] However, they have different dependencies on excitation light frequencies. Using a simple dipole oscillator model, it can be shown that, at resonance frequency, the real part shows a derivative-like shape, while the imaginary part peaks at the resonance frequency.[63] In our recent publication, we have verified that the IR near-field phase signal has very similar frequency dependence as that of the Fourier transform infrared vibrational peaks with sub-wavenumber agreement of

https://doi.org/10.1021/acs.jpcc.3c07693
J. Phys. Chem. C 2024, 128, 2052−2061

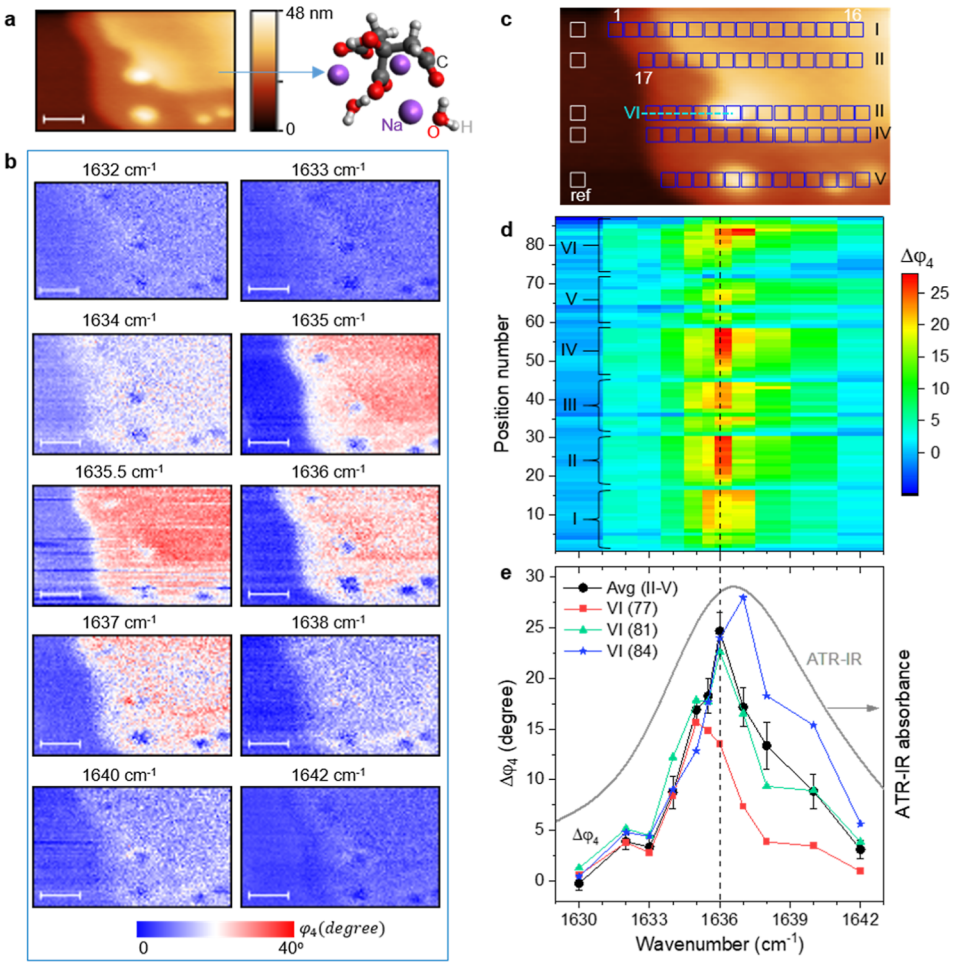

Figure 1. Vibrational nanoimaging of the water bending mode in a thin film. (a) Topographic image of an AuNC/Na_3Cit film deposited by drop-casting a colloidal aqueous solution. The inset on the right shows the structure of Na_3Cit dihydrate, which may serve as a fundamental unit in forming the film's structure. The scale bar is 200 nm. (b) IR s-SNOM vibrational images of the water bending mode at different QCL frequencies. The scale bar in the images is 200 nm. (c) Arrays of 5 pixels × 5 pixels in five rows (I–V) and a 2 pixel × 2 pixel (VI) area were selected for extracting the phase signal and evaluating the dependence of near-field spectra on nanoscale environments (one pixel is 10 nm). The white boxes on the left end are used as reference points in calculating the phase difference ($\Delta\varphi$) as described in the text. (d) Waterfall plot of the spectra extracted from the selected spots in (c), where each row represents the spectra of a spot. (e) Average near-field spectrum (black circles) and representative individual spectra extracted from the 2 pixel × 2 pixel spot (red squares, green triangles, and blue stars).

peak values.[55] As a result, the phase signal is used to track the vibrational resonance IR absorption in solid thin films. To evaluate the laser-frequency-dependent phase signal, a silicon wafer not coated by the sample is used as a reference. Thus, the phase difference is calculated as $\Delta\varphi_4 = \varphi_{4,\text{sample}} - \varphi_{\text{ref}}$.

3. RESULTS AND DISCUSSION

Evaporation-induced self-assembly of colloidal NCs results in a highly heterogeneous film characterized by significant variations in nanocrystal packing and excess ligand distribution from the center to the pinning point of the drop-cast solution. This heterogeneity offers advantages for studying the dependence of intermolecular interactions on various nanoscale environments. The far-field ATR-IR spectrum of the AuNC/Na_3Cit film is shown in Figure S2. In addition to the significant peak at 1558 cm^{-1} (attributed to the antisymmetric stretching mode of the carboxylate group of citrate), the presence of a peak at 1636.8 cm^{-1} is notable, corresponding to the water bending mode. Park et al. have previously reported the peak due to the water bending mode in citrate-capped AuNC films, demonstrating a decrease in peak intensity upon solvent evaporation.[31] Similarly, we have observed in the ATR-IR spectra of both Na_3Cit and sodium acetate films, measured before and after the completion of solvent (water) evaporation, that the peak at 1636.8 cm^{-1} is attributable to the water bending mode resonance (Figure S3).

The topographic image presented in Figure 1a reveals layers of Na_3Cit film, with four AuNCs visible in the topography and a fifth one becoming apparent in the phase images (Figure 1b). The same sample region depicted in Figure 1a is scanned at multiple QCL excitation frequencies ranging from 1630 to 1642 cm^{-1} with 0.5 and 1 cm^{-1} increments. The near-field IR phase images, obtained at the fourth harmonic of demodulation (φ_4), are displayed in Figure 1b.

The phase signal relative to the substrate (close to the left end) is weak at 1632 and 1633 cm^{-1}, becomes pronounced between 1634 and 1637 cm^{-1}, remains significant at 1638 and 1639 cm^{-1}, and returns to background levels at 1642 cm^{-1}. This signal attests to the presence of water molecules coordinated within the Na_3Cit film. The series of images suggests that absorption due to the water bending mode has a very narrow spectral window. It is important to note that while

https://doi.org/10.1021/acs.jpcc.3c07693
J. Phys. Chem. C 2024, 128, 2052−2061

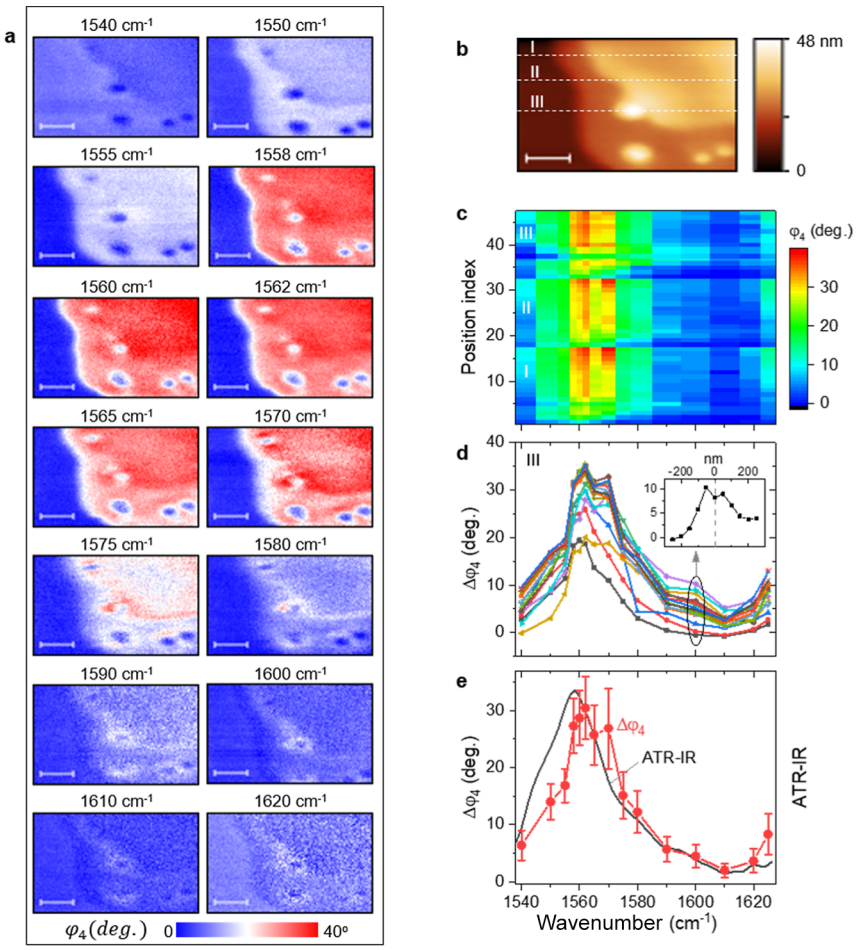

Figure 2. Vibrational nanoimaging of the antisymmetric stretching mode of citrate. (a) IR s-SNOM vibrational images at different QCL frequencies. The scale bar is 200 nm. (b) Corresponding topographic image. The three dashed lines show the rows from which near-field spectra are extracted using arrays of 5 pixel × 5 pixel area. (c) Waterfall plot showing the spectra extracted from the near-field images. Each row represents a spectrum extracted from one 5 pixel × 5 pixel area, and the left-to-right displacement in the topography corresponds to vertical ordering in the waterfall plot. (d) Individual spectra extracted from row III that crosses on the AuNC. The plots shown by black squares, red circles, and blue triangles are close to the edge of the thin film and show one major peak. With further crossing to a thicker region, a different peak grows at 1570 cm^{-1}. The inset plot shows the phase signal at 1600 cm^{-1} with respect to the displacement from the center of the AuNC. (e) Average near-field spectrum (red circles) compared with the far-field AIR-IR spectrum.

absorption from ambient water molecules at the solid−air interface is always possible at the ambient condition, this effect is not expected to generate phase contrast between the substrate and the Na_3Cit film. For more quantitative spectral analysis, we extracted a series of spectra from a 5 pixel × 5 pixel area to gain insights into how the water bending frequency is sensitive to nanoscale environments. To achieve this, arrays of spots in five rows, marked in Figure 1c, were selected with the white box close to the left end serving as a reference. In this analysis, the nanoparticles are used as the origin of coordinates, enabling extraction of the phase signal from the same area in images from different scans at the range of QCL frequencies. In addition to the arrays of 5 pixels × 5 pixels in the five rows, a sixth row of 2 pixels × 2 pixels (labeled VI in Figure 1c) was included to observe the averaging effect. Individual spectra obtained following these procedures are presented in Figure S4, while a waterfall plot containing all the spectra is shown in Figure 1d. Here, each row represents the spectrum of a spot marked in Figure 1c. Overall, the peak position fluctuates between 1635 and 1637 cm^{-1}, with an average peak at 1636 cm^{-1}. The representative near-field spectra, indicated by red squares, green triangles, and blue stars in Figure 1e, are from row VI. The trend illustrates the evolution of the peak position from 1635 cm^{-1} (for thin film regions) to 1637 cm^{-1}, which is close to but not at the center of the AuNC. We observe that at the center of the AuNC, the phase contrast decreases at nearly all QCL frequencies (see Figure 1b). This is due to the competition between tip-particle and tip-image dipole interactions.[55,64,65]

The line width of the far-field ATR-IR spectrum (indicated by the gray line in Figure 1e) is about 7 cm^{-1}. This is comparable to the line width found in gas-phase spectra of water clusters[6] and is significantly narrower than the line width (~37 cm^{-1}) observed in sum-frequency-generation spectra of bulk water surfaces.[66] If we consider the average near-field spectra (shown by the black solid circles in Figure 1e) as constituting a single peak, the line width is approximately 4 cm^{-1}. Upon closer examination of both the average and individual spectra, it becomes apparent that there are minor peaks on both the lower and higher energy sides of the major peak. While the number of near-field data points may be insufficient for determining the precise positions of these minor peaks, their existence is noteworthy. Considering that the bending mode frequency increases with hydrogen

https://doi.org/10.1021/acs.jpcc.3c07693
J. Phys. Chem. C 2024, 128, 2052−2061

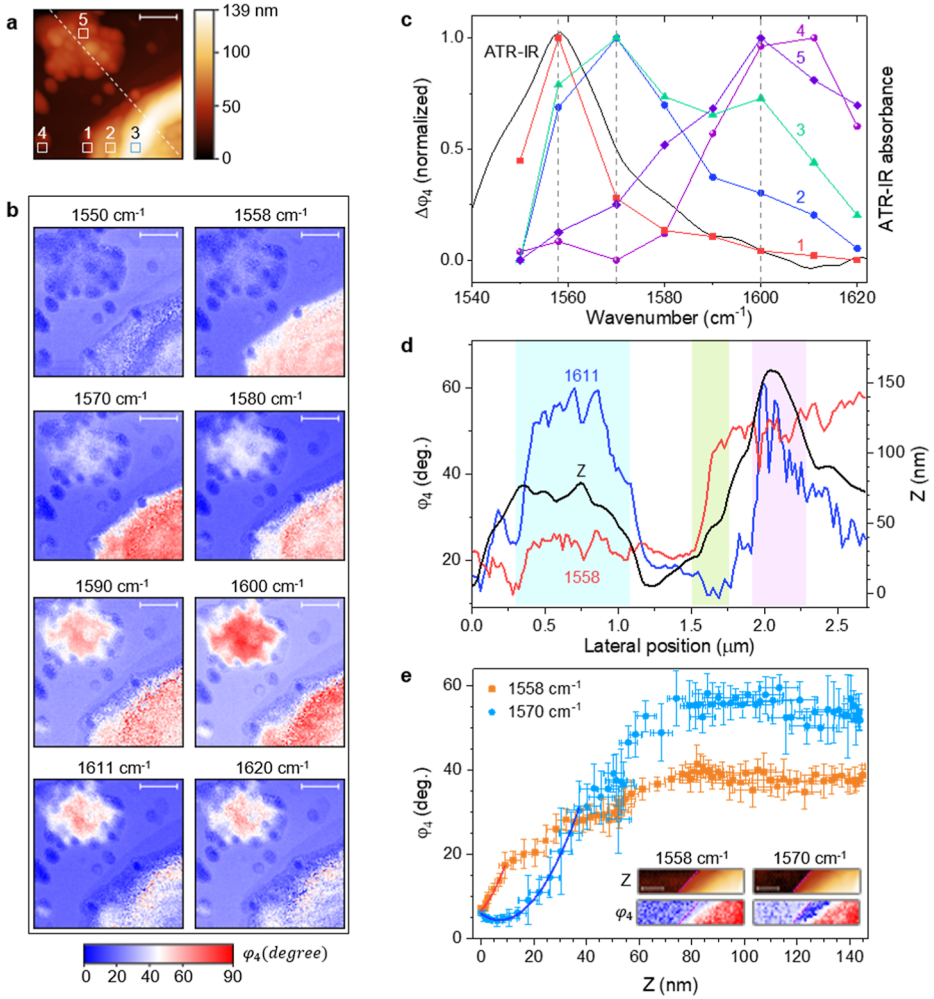

Figure 3. Identification of multiple structural domains through vibrational nanoimaging. (a) Topographic image showing a highly heterogeneous area and (b) corresponding IR s-SNOM phase images obtained at incremental laser frequencies. Scale bar 500 nm. (c) Near-field spectra from different locations labeled as 1, 2, 3, 4, and 5 on the topographic image (a). (d) IR phase (left axis) and topographic height (right axis) line profiles along the white dashed lines in (a). (e) Average phase signal plotted as a function of the average sample thickness at 1558 cm^{-1} (orange square) and 1570 cm^{-1} (blue circles). The solid lines are quadratic functions fit to the data to show the trend of the phase contrast as the sample thickness increases initially. The inset images show the region from which the line profiles are extracted to calculate the average values. The pink line in the inset images shows a bare substrate−film boundary, and at 1570 cm^{-1}, a negative phase contrast is observed before the film is sufficiently thick. The scale bar on the inset image is 200 nm.

bonding,[11] the lower-energy minor peak could be attributed to water molecules near the film−air interface. Conversely, the higher-energy peak could be due to water molecules at the substrate−film interface. The major band, likely arising from the inner layer of the film, has a line width narrower than 3 cm^{-1}. This is in surprising agreement with the line width of the rotationally resolved stretching mode of a water molecule in a $Li^+(H_2O)Ar$ complex,[10] although gas-phase data for the bending mode is not available. The line width observed in this experiment is much narrower than that typically expected for the condensed phase, considering reported values such as approximately 37 cm^{-1} for surface molecules of bulk water,[66] 60−83 cm^{-1} for liquid water depending on the experimental conditions,[4,7,67] and around 50 cm^{-1} for water molecules adsorbed on a gold electrode at an applied reduction potential.[68] The narrow line width in our study may be explained by the well-defined coordination in the Na_3Cit film, a structure likely influenced by the presence of the AuNCs. This hypothesis aligns with the recent observation of line width narrowing in the water-bending mode resonance in liquid water upon the addition of glycerol.[7] In the solid film, rotational degrees of freedom can be discounted, suggesting that the narrow line width may indicate a minimal effect of inhomogeneous broadening.

We now turn our attention to the sensitivity of the citrate carbonyl antisymmetric stretching mode to the nanoscale variations in intermolecular interactions that determine the structural heterogeneity of the film. In the far-field ATR-IR spectrum, the antisymmetric stretching mode has a major peak at 1558 cm^{-1}, and the corresponding near-field vibrational images are displayed in Figure 2a. At 1540 cm^{-1}, the phase signal in the thinner portion of the film is indistinguishable from that of the substrate, which exhibits a slightly higher phase signal compared to that of the thicker portion of the film. At 1550 cm^{-1}, all regions of the film (except for the areas with negative contrast due to the AuNCs) show a phase signal higher than that of the substrate. Furthermore, the thinner section continues to have a slightly higher phase signal than that of the thicker section. This observation hints a thickness-dependent structural variation that results in different vibra-

https://doi.org/10.1021/acs.jpcc.3c07693
J. Phys. Chem. C 2024, 128, 2052−2061

tional resonances. From 1555 to 1565 cm^{-1}, the film consistently shows a much higher phase signal compared with that of the substrate. Between 1570 and 1600 cm^{-1}, spatial variations in the phase signal are observed, which depend on the specific locations. Notably, a higher phase signal is observed at the boundary between the thin and thick layers, as well as around the AuNCs when the QCL frequency increases. At 1610 and 1620 cm^{-1}, the overall phase signal from the film is slightly lower than that of the substrate, except in the notably brighter regions surrounding the AuNC.

The waterfall plot in Figure 2c shows the near-field phase spectra extracted from arrays of 5 pixels × 5 pixels across the three dashed lines in Figure 2b. The corresponding individual spectra extracted from each spot and row are plotted in Figure S5. The spectra in Figures 2c and S5 show variation of the near-field spectra and the relative signal strength transitioning from the thin to the thick region of the film. The near-field plots (black squares, red circles, and blue triangles in Figure 2d) show one major peak at ∼1560 cm^{-1}, which is in reasonable agreement with the peak position (∼1558 cm^{-1}) observed in the ATR-IR spectra. Proceeding further into the thick film region, another peak develops at ∼1570 cm^{-1}, indicating the formation of a different structural domain as the film thickness increases. The IR phase signal at around 1600 cm^{-1} is generally weak but becomes relatively stronger near the AuNCs. The inset plot in Figure 2d illustrates that the IR phase signal at 1600 cm^{-1} decreases with distance from the edge of the AuNC. Overall, depending on the nanoscale environment, three resonances characteristic of the antisymmetric stretching vibrations of citrate are identified from spatiospectral analysis.

To gain further insight into the origin of the three resonances of the COO^- antisymmetric stretch, vibrational images of a more heterogeneous region (Figure 3a) are recorded at different QCL frequencies, and the results are displayed in Figure 3b. Five spots are selected to represent the variation within this scan region. From 1 to 3, the sample thickness increases significantly. Spot 4 represents an island of Na_3Cit film close to an AuNC. Spot 5 represents AuNC aggregates covered with Na_3Cit film. Close observation of the series of phase images in Figure 3b shows that the signal at the five spots has different dependencies on the excitation frequencies. For example, spot 1 (thinner than 2 and 3) has the strongest phase signal at 1558 cm^{-1}, and it decreases rapidly with the excitation frequency increasing further as shown by the red squares in Figure 3c. In spots 2 and 3, the phase signal has a maximum at 1570 cm^{-1} (blue squares and green triangles in Figure 3c), and spot 3 appears to show an additional peak at 1600 cm^{-1}. In spots 4 and 5, the phase signal increases as the QCL frequency increases to 1600 and 1611 cm^{-1} (purple sphere and violet diamond, respectively, in Figure 3c). Overall, the three stretching vibrational resonances of citrate observed in Figure 2 are reproduced in Figure 3.

The line profiles in Figure 3d (across the dashed line on the topographic image in Figure 3a) show the dependence of the vibrational resonance at 1600/1611 cm^{-1} on the proximity to the AuNCs as well as on thickness in comparison with the trend at 1558 cm^{-1}. In the region where the AuNCs are discernible in the topographic image (around spot 5, blue shade), the 1611 cm^{-1} phase signal is about 32° above the 1558 cm^{-1} signal, which is at the background level. In contrast, in the thin film region without the AuNC (Figure 3d, green shade), the 1558 cm^{-1} phase signal is about 32° higher than the 1611 cm^{-1} signal, which is below the background signal of the substrate, in contrast to the observation at spot 5. This spatially resolved chemical mapping establishes unambiguously that the Na_3Cit aggregate in the proximity of the AuNCs has an intermolecular interaction that results in a significant blue-shift of the COO^- antisymmetric vibrational frequency. However, the phase contrast at 1600/1611 cm^{-1} cannot be attributed to surface-bound COO^- as claimed in the past[31] because the molecular aggregate is clearly thicker than a monolayer. This is confirmed by analyzing the IR phase image of the island close to a single AuNC (spot 4, see also Figure S6). The size of the island in the proximity of the AuNC is over 20 nm, yet its IR phase signal is stronger at 1611 cm^{-1} than at 1558 cm^{-1} as shown by the solid purple sphere in Figure 3c. Clearly, the vibrational resonance around 1611 cm^{-1} should be attributed to surface-templated higher-order structure in Na_3Cit film as opposed to surface-bound COO^-.[31]

To confirm the existence of a distinct band around 1570 cm^{-1}, the average phase signals at 1558 and 1570 cm^{-1} are plotted as a function of topographic height (Z), considering a region free of AuNC (see inset images in Figure 3e). At 1558 cm^{-1}, the phase signal increases linearly with the initial increase of Z as shown by the orange square in Figure 3e and the corresponding linear fit (red line) to the data. On the other hand, at 1570 cm^{-1}, the phase signal has a quadratic trend that appears to decrease with Z initially below the background level before it increases rapidly. The lower-than-substrate phase signal for the ultrathin film at 1570 cm^{-1} is also observed in the inset phase image (Figure 3e) on the right side of the dashed pink line. With increasing Z, the 1570 cm^{-1} phase signal overtakes that of 1558 cm^{-1} (Figure 3e). Assuming a comparable oscillator strength of the vibrational modes, the higher phase signal at 1570 cm^{-1} for the thick sample may indicate a higher proportion of the corresponding structural domain. This observation may suggest that the vibrational resonance around 1570 cm^{-1} may be due to a subsurface structure that does not form until the film is sufficiently thick.

And yet, the most unambiguous and vivid evidence for the existence of a structural domain with vibrational resonance at ∼1570 cm^{-1} is obtained from a real-space mapping of adjacent sample planes (Figure 4a) with $Z > 15$ nm (region 1) and $Z < 5$ nm (region 2). At 1558 cm^{-1}, the phase signals at the two planes are comparable (Figure 4b), while the phase contrast in the $Z < 5$ nm region is completely absent at 1570 cm^{-1} (Figure 4c). The line profiles in Figure 4d show the thickness-dependent IR phase contrast at the two QCL frequencies more quantitatively. Clearly, the 1570 cm^{-1} signal appears when the sample is sufficiently thick, confirming the vibrational resonance of a subsurface structure. Additional results (obtained on different samples) that show the reproducibility of the identified resonances are available in the Supporting Information (see Figures S7 and S8).

Vibrational signatures of molecular species on the AuNC are obtained from SERS spectroscopy, which has inherent sensitivity to molecules directly adsorbed on the surface.[69] With the exception of the Raman inactive modes at 1558 and 1366 cm^{-1}, the Na_3Cit vibrational peaks observed in the SERS spectra are in agreement with the peak positions in the ATR-IR spectra within a wavenumber (Figure 5a,b). Considering that the ATR-IR spectrum is characteristic of the bulk phase, the close agreement between the corresponding IR and SERS peak positions indicates a weak interaction of citrate with the gold surface. The SERS peaks are narrower than the corresponding

https://doi.org/10.1021/acs.jpcc.3c07693
J. Phys. Chem. C 2024, 128, 2052−2061

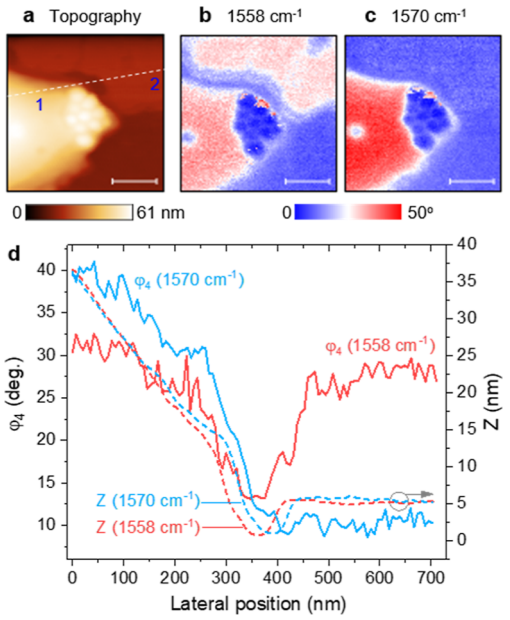

Figure 4. ON and OFF IR phase signals depending on sample thickness. (a) Topographic image of AuNCs/Na_3 Cit film showing regions of varying thickness—thick (labeled 1) and thin (labeled 2). (b) Phase signals in these two regions are comparable at an excitation frequency of 1558 cm^{-1}. (c) Phase signal from the thinner region (region 2) is completely absent at an excitation of 1570 cm^{-1}. (d) Linepprofiles along the white dashed line in (a) indicate that for lateral positions ranging from 450−700 nm, the sample thickness is just under 5 nm (right axis, dashed red and blue lines), and the phase signal at 1570 cm^{-1} is at the background level (blue line), in contrast to the pronounced phase signal at 1558 cm^{-1}. A scale bar of 200 nm applies to all images.

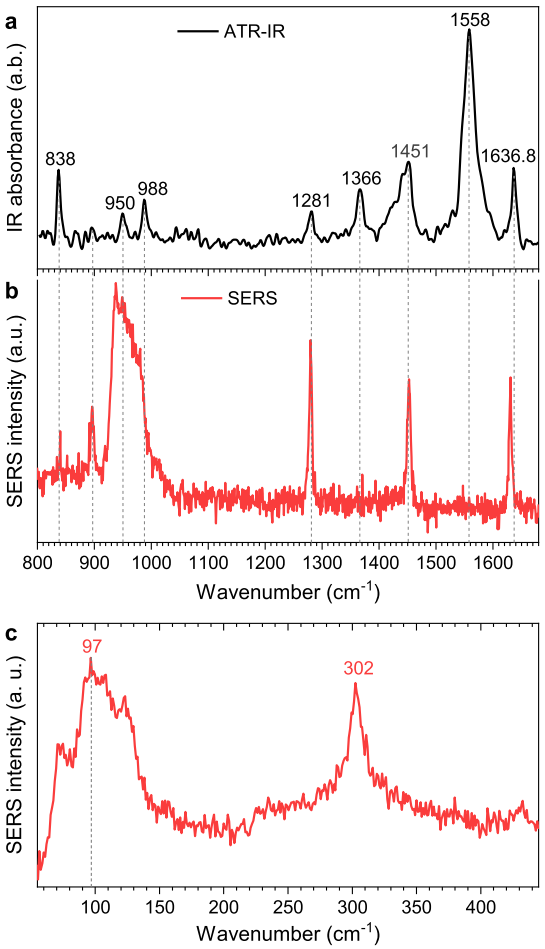

Figure 5. Identifying surface-bound chemical species. (a) ATR-IR spectrum of an AuNC/Na_3Cit film deposited on a silicon wafer. (b) SERS spectrum of the same sample. Vertical dashed lines are drawn at the ATR-IR peak positions and align with the corresponding peaks in the SERS spectrum, except for the peak at 1636.8 cm^{-1} (water bending mode), which is downshifted by approximately 6 cm^{-1}. (c) SERS spectrum in the low-frequency spectral window showing the Au−O interaction at 302 cm^{-1}. The multiple peaks around 97 cm^{-1} may be due to a metal cluster that involves hydrated Na^+ and surface Au atom.

ATR-IR peaks, indicating the sensitivity of SERS to surface species. The SERS peak at 1631 cm^{-1} is close to the water bending resonance observed in the ATR-IR spectrum with about 6 cm^{-1} downshift, which may indicate water molecules bound to the surface through the O atom. The more significant frequency shift of the water bending resonance compared to any of the citrate peaks also suggests that water molecules mediate the interaction of citrate with the surface. The Raman peak at 302 cm^{-1} (Figure 5c) further confirms Au−O interaction in agreement with the reported results.[70] The low-frequency peaks in the 72−123 cm^{-1} region in Figure 5c may indicate a metal cluster of surface Au atom and Na^+ cation stabilized by water, suggesting that citrate interacts with the surface through the $Na^+(H_2O)_n$ group.

In our discussion thus far, we have observed multiple vibrational resonance frequencies, each stemming from the antisymmetric citrate carbonyl stretching mode, attributed to variations in nanoscale environments. To gain a molecular-level understanding and propose the origin of these observed resonances, we performed DFT calculations. These calculations were conducted at the B3LYP/aug-cc-pVDZ level using Gaussian 16, with the aim of elucidating the detailed molecular interactions at play. Comparing the vibrational spectra of citrate and Na_3Cit shows that the ionic interaction results in a blue shift of over 50 cm^{-1} in both the symmetric and antisymmetric stretching mode frequencies (Figure S9). For further analysis of the intermolecular interaction, including hydrogen-bonding, sodium acetate is used as a surrogate model system to simplify the calculation, considering the similarity of the spectra for the two species (Figure S3). The antisymmetric stretching frequency that appears at 1566 cm^{-1} for the monomer is blue-shifted to 1630 cm^{-1} (Figure 6a,d). The 64 cm^{-1} upshift is comparable to the difference between the experimentally observed peak position at 1558 and 1611 cm^{-1}, suggesting that an AuNC serves as a template to induce a higher-order stacking structure in the Na_3Cit aggregate. Adding up to two water molecules results in red shifting in both the monomer- (Figure 6a−c) and dimer- (Figure 6d−f) based structures. In this regard, the structural domain that gives rise to a vibrational peak at 1570 cm^{-1} may have a similar higher-order structure as the 1611 cm^{-1} domain, where the downshift indicates a higher extent of hydrogen bonding in the subsurface.

The proposed weak interaction of the carboxylate functional group with AuNCs, mediated by sodium cations and water molecules, aligns with recent observations of methylene blue (MB) SERS spectra adsorbed on gold nanoparticles with cetyltrimethylammonium bromide (CTAB) and carboxylate surface ligands.[27] It was discovered that the MB SERS spectra

https://doi.org/10.1021/acs.jpcc.3c07693
J. Phys. Chem. C 2024, 128, 2052−2061

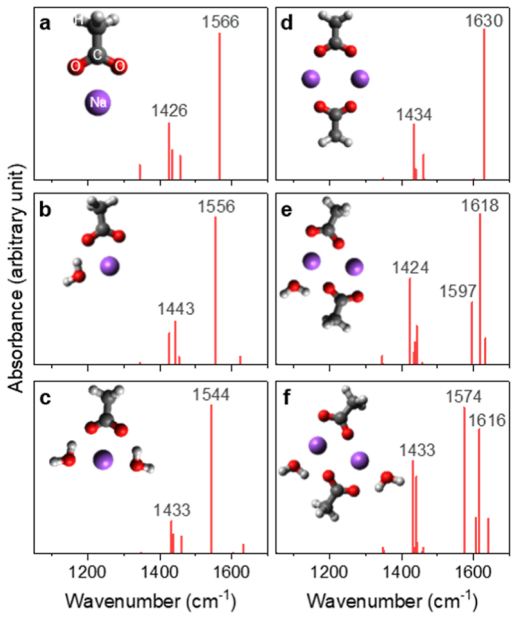

Figure 6. Results of DFT calculations using sodium acetate as a surrogate for Na_3Cit. IR spectra of (a–c) a monomer and (d–f) a dimer with an increasing number of water molecules forming hydrogen bonding. The optimized structures are displayed as insets in the panels that show the corresponding spectra.

from gold nanoparticles with carboxylate surface ligands are similar to those obtained when MB is adsorbed on bare gold nanoislands without surface ligands (prepared by electron-beam evaporation). However, there is a significant difference compared with the spectra of MB adsorbed on gold nanoparticles with CTAB surface ligands. This observation suggests that MB can replace carboxylate-based surface ligands, indicating a weak ligand–surface interaction. Additionally, it has been noted that plasmon-driven MB N-demethylation, thought to involve singlet oxygen generation,[71−73] is inefficient when gold nanoparticles with carboxylate surface ligands are used. This implies the direct adsorption of MB onto the metal surface, replacing the surface ligand and leading to efficient molecular excitation energy transfer to the metal surface, which, in turn, suppresses the generation of singlet oxygen.

4. CONCLUSIONS

In conclusion, the combination of s-SNOM with a tunable IR QCL has provided a powerful method for imaging and understanding molecular vibrations in complex nanostructured materials. Through spatiospectral imaging of thin films of colloidal AuNCs with Na_3Cit ligands at ambient conditions, we have demonstrated the ability to resolve the water bending mode with a line width of less than 3 cm^{-1}, closely matching gas-phase spectral values. Our analysis has also revealed the presence of three partially resolved domains by examining the water bending mode near-field spectra, elucidating variations at the film–air interface, within the inner layer, and at the film–substrate interface. These domains highlight the intricate structure of the films and the complex interactions occurring at different depths. Investigations into the citrate stretching mode have yielded insights into three distinct structural domains associated with proximity to AuNCs and Na_3Cit film thickness. These findings challenge previous spectral interpretations, uncovering that certain vibrational bands originate not from surface-bound carboxylates but rather from higher-order structures within the thick Na_3Cit aggregates. Furthermore, through SERS analysis, we have clarified the nature of binding of citrate to NCs, which is facilitated by sodium ions and water molecules, providing a more comprehensive understanding of the interfacial chemistry at play. The experimental findings are supported by DFT calculations, which confirm the spectral assignments. This research contributes to the advancement of structural elucidation in solid films, offering new perspectives on the nanoscale variation of intermolecular interactions and fostering the development of novel nanomaterials with precisely engineered properties.

■ ASSOCIATED CONTENT

Supporting Information

The Supporting Information is available free of charge at https://pubs.acs.org/doi/10.1021/acs.jpcc.3c07693.

Additional near-field phase images of AuNCs/Na_3Cit film and ATR-IR spectra of sodium acetate and trisodium citrate (PDF)

■ AUTHOR INFORMATION

Corresponding Author

Terefe G. Habteyes − *Department of Chemistry and Chemical Biology, University of New Mexico, Albuquerque, New Mexico 87131, United States;* orcid.org/0000-0001-5978-6464; Email: habteyes@unm.edu

Author

Wassie M. Takele − *Department of Chemistry and Chemical Biology, University of New Mexico, Albuquerque, New Mexico 87131, United States*

Complete contact information is available at: https://pubs.acs.org/10.1021/acs.jpcc.3c07693

Notes

The authors declare no competing financial interest.

■ ACKNOWLEDGMENTS

This work has been supported by the National Science Foundation Award no. 2154617.

■ ABBREVIATIONS

s-SNOM, scattering-type scanning near-field optical microscope; SERS, surface-enhanced Raman scattering; ATR-IR, attenuated total reflectance infrared; QCL, quantum cascade laser; AuNC, gold nanocrystal; Na_3Cit, trisodium citrate; DFT, density functional theory

■ REFERENCES

(1) Seki, T.; Chiang, K.-Y.; Yu, C.-C.; Yu, X.; Okuno, M.; Hunger, J.; Nagata, Y.; Bonn, M. The Bending Mode of Water: A Powerful Probe for Hydrogen Bond Structure of Aqueous Systems. *J. Phys. Chem. Lett.* **2020**, *11*, 8459−8469.

(2) Stiopkin, I. V.; Weeraman, C.; Pieniazek, P. A.; Shalhout, F. Y.; Skinner, J. L.; Benderskii, A. V. Hydrogen Bonding at the Water Surface Revealed by Isotopic Dilution Spectroscopy. *Nature* **2011**, *474*, 192−195.

(3) Ni, Y.; Skinner, J. L. Ir and Sfg Vibrational Spectroscopy of the Water Bend in the Bulk Liquid and at the Liquid-Vapor Interface, Respectively. *J. Chem. Phys.* **2015**, *143*, 014502.

(4) Ashihara, S.; Fujioka, S.; Shibuya, K. Temperature Dependence of Vibrational Relaxation of the Oh Bending Excitation in Liquid H2o. *Chem. Phys. Lett.* **2011**, *502*, 57−62.

(5) Yu, C.-C.; Chiang, K.-Y.; Okuno, M.; Seki, T.; Ohto, T.; Yu, X.; Korepanov, V.; Hamaguchi, H.-o.; Bonn, M.; Hunger, J.; Nagata, Y. Vibrational Couplings and Energy Transfer Pathways of Water's Bending Mode. *Nat. Commun.* **2020**, *11*, 5977.
(6) Zhang, B.; Yu, Y.; Zhang, Y.-Y.; Jiang, S.; Li, Q.; Hu, H.-S.; Li, G.; Zhao, Z.; Wang, C.; Xie, H.; Zhang, W.; Dai, D.; Wu, G.; Zhang, D. H.; Jiang, L.; Li, J.; Yang, X. Infrared Spectroscopy of Neutral Water Clusters at Finite Temperature: Evidence for a Noncyclic Pentamer. *Proc. Natl. Acad. Sci. U.S.A.* **2020**, *117*, 15423−15428.
(7) Morita, M.; Matsumura, F.; Shikata, T.; Ogawa, Y.; Kondo, N.; Shiraga, K. Hydrogen-Bond Configurations of Hydration Water around Glycerol Investigated by Hoh Bending and Oh Stretching Analysis. *J. Phys. Chem. B* **2022**, *126*, 9871−9880.
(8) Devlin, J. P.; Sadlej, J.; Buch, V. Infrared Spectra of Large H2o Clusters: New Understanding of the Elusive Bending Mode of Ice. *J. Phys. Chem. A* **2001**, *105*, 974−983.
(9) Patwari, G. N.; Lisy, J. M. Mimicking the Solvation of Aqueous Na+ in the Gas Phase. *J. Chem. Phys.* **2003**, *118*, 8555−8558.
(10) Vaden, T. D.; Lisy, J. M.; Carnegie, P. D.; Dinesh Pillai, E.; Duncan, M. A. Infrared Spectroscopy of the Li+(H2o)Ar Complex: The Role of Internal Energy and Its Dependence on Ion Preparation. *Phys. Chem. Chem. Phys.* **2006**, *8*, 3078−3082.
(11) Falk, M. The Frequency of the HOH Bending Fundamental in Solids and Liquids. *Spectrochim. Acta, Part A* **1984**, *40*, 43−48.
(12) Yin, Y.; Alivisatos, A. P. Colloidal Nanocrystal Synthesis and the Organic-Inorganic Interface. *Nature* **2005**, *437*, 664−670.
(13) Kwan Li, K.; Wu, C.-Y.; Yang, T.-H.; Qin, D.; Xia, Y. Quantification, Exchange, and Removal of Surface Ligands on Noble-Metal Nanocrystals. *Acc. Chem. Res.* **2023**, *56*, 1517−1527.
(14) Mark, L. O.; Zhu, C.; Medlin, J. W.; Heinz, H. Understanding the Surface Reactivity of Ligand-Protected Metal Nanoparticles for Biomass Upgrading. *ACS Catal.* **2020**, *10*, 5462−5474.
(15) Ansar, S. M.; Kitchens, C. L. Impact of Gold Nanoparticle Stabilizing Ligands on the Colloidal Catalytic Reduction of 4-Nitrophenol. *ACS Catal.* **2016**, *6*, 5553−5560.
(16) Vu, K. B.; Bukhryakov, K. V.; Anjum, D. H.; Rodionov, V. O. Surface-Bound Ligands Modulate Chemoselectivity and Activity of a Bimetallic Nanoparticle Catalyst. *ACS Catal.* **2015**, *5*, 2529−2533.
(17) Ben-Shahar, Y.; Scotognella, F.; Waiskopf, N.; Kriegel, I.; Dal Conte, S.; Cerullo, G.; Banin, U. Effect of Surface Coating on the Photocatalytic Function of Hybrid Cds-Au Nanorods. *Small* **2015**, *11*, 462−471.
(18) Cirri, A.; Silakov, A.; Jensen, L.; Lear, B. J. Probing Ligand-Induced Modulation of Metallic States in Small Gold Nanoparticles Using Conduction Electron Spin Resonance. *Phys. Chem. Chem. Phys.* **2016**, *18*, 25443−25451.
(19) Jain, V.; Roy, S.; Roy, P.; Pillai, P. P. When Design Meets Function: The Prodigious Role of Surface Ligands in Regulating Nanoparticle Chemistry. *Chem. Mater.* **2022**, *34*, 7579−7597.
(20) Liyanage, T.; Nagaraju, M.; Johnson, M.; Muhoberac, B. B.; Sardar, R. Reversible Tuning of the Plasmoelectric Effect in Noble Metal Nanostructures through Manipulation of Organic Ligand Energy Levels. *Nano Lett.* **2020**, *20*, 192−200.
(21) Schürmann, R.; Titov, E.; Ebel, K.; Kogikoski, S.; Mostafa, A.; Saalfrank, P.; Milosavljević, A. R.; Bald, I. The Electronic Structure of the Metal-Organic Interface of Isolated Ligand Coated Gold Nanoparticles. *Nanoscale Adv.* **2022**, *4*, 1599−1607.
(22) Zhang, W.; Qin, R.; Fu, G.; Zheng, N. Hydrogen Bond Network Induced by Surface Ligands Shifts the Semi-Hydrogenation Selectivity over Palladium Catalysts. *J. Am. Chem. Soc.* **2023**, *145*, 10178−10186.
(23) Lu, L.; Zou, S.; Fang, B. The Critical Impacts of Ligands on Heterogeneous Nanocatalysis: A Review. *ACS Catal.* **2021**, *11*, 6020−6058.
(24) Cargnello, M. Colloidal Nanocrystals as Building Blocks for Well-Defined Heterogeneous Catalysts. *Chem. Mater.* **2019**, *31*, 576−596.
(25) Kim, D.; Kim, J.; Park, Y. I.; Lee, N.; Hyeon, T. Recent Development of Inorganic Nanoparticles for Biomedical Imaging. *ACS Cent. Sci.* **2018**, *4*, 324−336.
(26) Langer, J.; Jimenez de Aberasturi, D.; Aizpurua, J.; Alvarez-Puebla, R. A.; Auguié, B.; Baumberg, J. J.; Bazan, G. C.; Bell, S. E. J.; Boisen, A.; Brolo, A. G.; et al. Present and Future of Surface-Enhanced Raman Scattering. *ACS Nano* **2020**, *14*, 28−117.
(27) Kookhaee, H.; Tesema, T. E.; Habteyes, T. G. Switching a Plasmon-Driven Reaction Mechanism from Charge Transfer to Adsorbate Electronic Excitation Using Surface Ligands. *J. Phys. Chem. C* **2020**, *124*, 22711−22720.
(28) Kafle, B.; Poveda, M.; Habteyes, T. G. Surface Ligand-Mediated Plasmon-Driven Photochemical Reactions. *J. Phys. Chem. Lett.* **2017**, *8*, 890−894.
(29) Habteyes, T. Anions as Intermediates in Plasmon Enhanced Photocatalytic Reactions. *J. Phys. Chem. C* **2020**, *124*, 26554−26564.
(30) Li, Z.; Zhang, C.; Sheng, H.; Wang, J.; Zhu, Y.; Yu, L.; Wang, J.; Peng, Q.; Lu, G. Molecular Cocatalyst of P-Mercaptophenylboronic Acid Boosts the Plasmon-Mediated Reduction of P-Nitrothiophenol. *ACS Appl. Mater. Interfaces* **2022**, *14*, 38302−38310.
(31) Park, J.-W.; Shumaker-Parry, J. S. Structural Study of Citrate Layers on Gold Nanoparticles: Role of Intermolecular Interactions in Stabilizing Nanoparticles. *J. Am. Chem. Soc.* **2014**, *136*, 1907−1921.
(32) Kawai, T.; Neivandt, D. J.; Davies, P. B. Sum Frequency Generation on Surfactant-Coated Gold Nanoparticles. *J. Am. Chem. Soc.* **2000**, *122*, 12031−12032.
(33) Weeraman, C.; Yatawara, A. K.; Bordenyuk, A. N.; Benderskii, A. V. Effect of Nanoscale Geometry on Molecular Conformation: Vibrational Sum-Frequency Generation of Alkanethiols on Gold Nanoparticles. *J. Am. Chem. Soc.* **2006**, *128*, 14244−14245.
(34) Lu, Z.; Karakoti, A.; Velarde, L.; Wang, W.; Yang, P.; Thevuthasan, S.; Wang, H.-f. Dissociative Binding of Carboxylic Acid Ligand on Nanoceria Surface in Aqueous Solution: A Joint in Situ Spectroscopic Characterization and First-Principles Study. *J. Phys. Chem. C* **2013**, *117*, 24329−24338.
(35) Dalstein, L.; Humbert, C.; Ben Haddada, M.; Boujday, S.; Barbillon, G.; Busson, B. The Prevailing Role of Hotspots in Plasmon-Enhanced Sum-Frequency Generation Spectroscopy. *J. Phys. Chem. Lett.* **2019**, *10*, 7706−7711.
(36) Torelli, M. D.; Putans, R. A.; Tan, Y.; Lohse, S. E.; Murphy, C. J.; Hamers, R. J. Quantitative Determination of Ligand Densities on Nanomaterials by X-Ray Photoelectron Spectroscopy. *ACS Appl. Mater. Interfaces* **2015**, *7*, 1720−1725.
(37) Liu, X.; Yu, M.; Kim, H.; Mameli, M.; Stellacci, F. Determination of Monolayer-Protected Gold Nanoparticle Ligand-Shell Morphology Using Nmr. *Nat. Commun.* **2012**, *3*, 1182.
(38) Guzman-Juarez, B.; Abdelaal, A. B.; Reven, L. Nmr Characterization of Nanoscale Surface Patterning in Mixed Ligand Nanoparticles. *ACS Nano* **2022**, *16*, 20116−20128.
(39) Zhang, Z.; Li, Y.; Frisch, J.; Bär, M.; Rappich, J.; Kneipp, J. In Situ Surface-Enhanced Raman Scattering Shows Ligand-Enhanced Hot Electron Harvesting on Silver, Gold, and Copper Nanoparticles. *J. Catal.* **2020**, *383*, 153−159.
(40) Grys, D.-B.; de Nijs, B.; Salmon, A. R.; Huang, J.; Wang, W.; Chen, W.-H.; Scherman, O. A.; Baumberg, J. J. Citrate Coordination and Bridging of Gold Nanoparticles: The Role of Gold Adatoms in Aunp Aging. *ACS Nano* **2020**, *14*, 8689−8696.
(41) Habteyes, T. G. Direct near-Field Observation of Orientation-Dependent Optical Response of Gold Nanorods. *J. Phys. Chem. C* **2014**, *118*, 9119−9127.
(42) Kiesow, K. I.; Dhuey, S.; Habteyes, T. G. Mapping near-Field Localization in Plasmonic Optical Nanoantennas with 10 Nm Spatial Resolution. *Appl. Phys. Lett.* **2014**, *105*, 053105.
(43) Habteyes, T. G.; Dhuey, S.; Kiesow, K. I.; Vold, A. Probe-Sample Optical Interaction: Size and Wavelength Dependence in Localized Plasmon near-Field Imaging. *Opt. Express* **2013**, *21*, 21607.
(44) Hu, F.; Luan, Y.; Fei, Z.; Palubski, I. Z.; Goldflam, M. D.; Dai, S.; Wu, J. S.; Post, K. W.; Janssen, G.; Fogler, M. M.; Basov, D. N.

https://doi.org/10.1021/acs.jpcc.3c07693
J. Phys. Chem. C 2024, 128, 2052−2061

Imaging the Localized Plasmon Resonance Modes in Graphene Nanoribbons. *Nano Lett.* **2017**, *17*, 5423−5428.
(45) Kim, D. S.; Heo, J.; Ahn, S. H.; Han, S. W.; Yun, W. S.; Kim, Z. H. Real-Space Mapping of the Strongly Coupled Plasmons of Nanoparticle Dimers. *Nano Lett.* **2009**, *9*, 3619−3625.
(46) Mastel, S.; Grefe, S. E.; Cross, G. B.; Taber, A.; Dhuey, S.; Cabrini, S.; Schuck, P. J.; Abate, Y. Real-Space Mapping of Nanoplasmonic Hotspots Via Optical Antenna-Gap Loading. *Appl. Phys. Lett.* **2012**, *101*, 131102.
(47) Rang, M.; Jones, A. C.; Zhou, F.; Li, Z. Y.; Wiley, B. J.; Xia, Y. N.; Raschke, M. B. Optical near-Field Mapping of Plasmonic Nanoprisms. *Nano Lett.* **2008**, *8*, 3357−3363.
(48) Dai, S. Y.; Ma, Q.; Yang, Y. F.; Rosenfeld, J.; Goldflam, M. D.; McLeod, A.; Sun, Z. Y.; Andersen, T. I.; Fei, Z.; Liu, M. K.; Shao, Y.; Watanabe, K.; Taniguchi, T.; Thiemens, M.; Keilmann, F.; Jarillo-Herrero, P.; Fogler, M. M.; Basov, D. N. Efficiency of Launching Highly Confined Polaritons by Infrared Light Incident on a Hyperbolic Material. *Nano Lett.* **2017**, *17*, 5285−5290.
(49) Dai, S.; Fei, Z.; Ma, Q.; Rodin, A. S.; Wagner, M.; McLeod, A. S.; Liu, M. K.; Gannett, W.; Regan, W.; Watanabe, K.; Taniguchi, T.; Thiemens, M.; Dominguez, G.; Neto, A. H. C.; Zettl, A.; Keilmann, F.; Jarillo-Herrero, P.; Fogler, M. M.; Basov, D. N. Tunable Phonon Polaritons in Atomically Thin Van Der Waals Crystals of Boron Nitride. *Science* **2014**, *343*, 1125−1129.
(50) Fali, A.; White, S. T.; Folland, T. G.; He, M. Z.; Aghamiri, N. A.; Liu, S.; Edgar, J. H.; Caldwell, J. D.; Haglund, R. F.; Abate, Y. Refractive Index-Based Control of Hyperbolic Phonon-Polariton Propagation. *Nano Lett.* **2019**, *19*, 7725−7734.
(51) Bylinkin, A.; Schnell, M.; Autore, M.; Calavalle, F.; Li, P.; Taboada-Gutièrrez, J.; Liu, S.; Edgar, J. H.; Casanova, F.; Hueso, L. E.; Alonso-Gonzalez, P.; Nikitin, A. Y.; Hillenbrand, R. Real-Space Observation of Vibrational Strong Coupling between Propagating Phonon Polaritons and Organic Molecules. *Nat. Photonics* **2021**, *15*, 197−202.
(52) Goikoetxea, M.; Amenabar, I.; Chimenti, S.; Paulis, M.; Leiza, J. R.; Hillenbrand, R. Cross-Sectional Chemical Nanoimaging of Composite Polymer Nanoparticles by Infrared Nanospectroscopy. *Macromolecules* **2021**, *54*, 995−1005.
(53) Choi, B.; Jeong, G.; Shin, H.-H.; Kim, Z. H. Molecular Vibrational Imaging at Nanoscale. *J. Chem. Phys.* **2022**, *156*, 160902.
(54) Tesema, T. E.; McFarland-Porter, R.; Zerai, E.; Grey, J.; Habteyes, T. G. Hierarchical Self-Assembly and Chemical Imaging of Nanoscale Domains in Polymer Blend Thin Films. *J. Phys. Chem. C* **2022**, *126*, 7764−7772.
(55) Wang, C.-F.; Kafle, B.; Tesema, T. E.; Kookhaee, H.; Habteyes, T. G. Molecular Sensitivity of near-Field Vibrational Infrared Imaging. *J. Phys. Chem. C* **2020**, *124*, 21018−21026.
(56) Habteyes, T. G.; Westphal, E. R.; Plackowski, K. M.; Kotula, P. G.; Meyerson, M. L.; White, S. L.; Corbin, W. C.; Ghosh, K.; Grey, J. K. Hierarchical Self-Assembly of Carbon Dots into High-Aspect-Ratio Nanowires. *Nano Lett.* **2023**, *23*, 9474−9481.
(57) Berweger, S.; Nguyen, D. M.; Muller, E. A.; Bechtel, H. A.; Perkins, T. T.; Raschke, M. B. Nano-Chemical Infrared Imaging of Membrane Proteins in Lipid Bilayers. *J. Am. Chem. Soc.* **2013**, *135*, 18292−18295.
(58) Abate, Y.; Akinwande, D.; Gamage, S.; Wang, H.; Snure, M.; Poudel, N.; Cronin, S. B. Recent Progress on Stability and Passivation of Black Phosphorus. *Adv. Mater.* **2018**, *30*, 1704749.
(59) Yalcin, S. E.; Legg, B. A.; Yeşilbaş, M.; Malvankar, N. S.; Boily, J.-F. Direct Observation of Anisotropic Growth of Water Films on Minerals Driven by Defects and Surface Tension. *Sci. Adv.* **2020**, *6*, No. eaaz9708.
(60) Kaltenecker, K. J.; Gölz, T.; Bau, E.; Keilmann, F. Infrared-Spectroscopic, Dynamic near-Field Microscopy of Living Cells and Nanoparticles in Water. *Sci. Rep.* **2021**, *11*, 21860.
(61) Ocelic, N.; Huber, A.; Hillenbrand, R. Pseudoheterodyne Detection for Background-Free near-Field Spectroscopy. *Appl. Phys. Lett.* **2006**, *89*, 101124.
(62) Bohren, C. F.; Huffman, D. R. *Absorption and Scattering of Light by Small Particles*; Wiley VCH: Weinheim, 2004.
(63) Fox, M. *Optical Properties of Solids*, 2nd ed.; Oxford University Press, 2010.
(64) Cvitkovic, A.; Ocelic, N.; Aizpurua, J.; Guckenberger, R.; Hillenbrand, R. Infrared Imaging of Single Nanoparticles Via Strong Field Enhancement in a Scanning Nanogap. *Phys. Rev. Lett.* **2006**, *97*, 060801.
(65) Kim, Z. H.; Ahn, S. H.; Liu, B.; Leone, S. R. Nanometer-Scale Dielectric Imaging of Semiconductor Nanoparticles: Size-Dependent Dipolar Coupling and Contrast Reversal. *Nano Lett.* **2007**, *7*, 2258−2262.
(66) Vinaykin, M.; Benderskii, A. V. Vibrational Sum-Frequency Spectrum of the Water Bend at the Air/Water Interface. *J. Phys. Chem. Lett.* **2012**, *3*, 3348−3352.
(67) Chuntonov, L.; Kumar, R.; Kuroda, D. G. Non-Linear Infrared Spectroscopy of the Water Bending Mode: Direct Experimental Evidence of Hydration Shell Reorganization? *Phys. Chem. Chem. Phys.* **2014**, *16*, 13172−13181.
(68) Li, J.-F.; Huang, Y.-F.; Duan, S.; Pang, R.; Wu, D.-Y.; Ren, B.; Xu, X.; Tian, Z.-Q. Sers and Dft Study of Water on Metal Cathodes of Silver, Gold and Platinum Nanoparticles. *Phys. Chem. Chem. Phys.* **2010**, *12*, 2493−2502.
(69) Masango, S. S.; Hackler, R. A.; Large, N.; Henry, A. I.; McAnally, M. O.; Schatz, G. C.; Stair, P. C.; Van Duyne, R. P. High-Resolution Distance Dependence Study of Surface-Enhanced Raman Scattering Enabled by Atomic Layer Deposition. *Nano Lett.* **2016**, *16*, 4251−4259.
(70) Li, C.-Y.; Dong, J.-C.; Jin, X.; Chen, S.; Panneerselvam, R.; Rudnev, A. V.; Yang, Z.-L.; Li, J.-F.; Wandlowski, T.; Tian, Z.-Q. In Situ Monitoring of Electrooxidation Processes at Gold Single Crystal Surfaces Using Shell-Isolated Nanoparticle-Enhanced Raman Spectroscopy. *J. Am. Chem. Soc.* **2015**, *137*, 7648−7651.
(71) Tesema, T. E.; Kafle, B.; Habteyes, T. G. Plasmon-Driven Reaction Mechanisms: Hot Electron Transfer Versus Plasmon-Pumped Adsorbate Excitation. *J. Phys. Chem. C* **2019**, *123*, 8469−8483.
(72) Tesema, T. E.; Annesley, C.; Habteyes, T. G. Plasmon-Enhanced Autocatalytic N-Demethylation. *J. Phys. Chem. C* **2018**, *122*, 19831−19841.
(73) Tesema, T. E.; Kafle, B.; Tadesse, M. G.; Habteyes, T. G. Plasmon-Enhanced Resonant Excitation and Demethylation of Methylene Blue. *J. Phys. Chem. C* **2017**, *121*, 7421−7428.

https://doi.org/10.1021/acs.jpcc.3c07693
J. Phys. Chem. C 2024, 128, 2052−2061